ADVANCED FUNCTIONAL MATERIALS
www.afm-journal.de

Graphene Solution-Gated Field-Effect Transistor Array for Sensing Applications

By *Markus Dankerl, Moritz V. Hauf, Andreas Lippert, Lucas H. Hess, Stefan Birner, Ian D. Sharp, Ather Mahmood, Pierre Mallet, Jean-Yves Veuillen, Martin Stutzmann,* and *Jose A. Garrido**

Graphene, with its unique combination of physical and electronic properties, holds great promise for biosensor and bioelectronic applications. In this respect, the development of graphene solution-gated field-effect transistor (SGFET) arrays capable of operation in aqueous environments will establish the real potential of graphene in this rapidly emerging field. Here, we report on a facile route for the scalable fabrication of such graphene transistor arrays and provide a comprehensive characterization of their operation in aqueous electrolytes. An on-chip structure for Hall-effect measurements allows the direct determination of charge carrier concentrations and mobilities under electrolyte gate control. The effect of the solution-gate potential on the electronic properties of graphene is explained using a model that considers the microscopic structure of water at the graphene/electrolyte interface. The graphene SGFETs exhibit a high transconductance and correspondingly high sensitivity, together with an effective gate noise as low as tens of μV. Our study demonstrates that graphene SGFETs, with their facile technology, high transconductance, and low noise promise to far outperform state-of-the-art Si-based devices for biosensor and bioelectronic applications.

1. Introduction

Biosensors and bioelectronics are called upon to provide valuable benefits for society in vital fields such as health care, security, and life sciences. Despite significant progress in recent years, this field is still in an early stage, and crucial topics such as the choice of the "optimum" bio-material and the development of electronic-based sensing techniques are still under consideration.[1–10] So far, silicon is the most commonly used material in this field due to its technological maturity,[1–3] although new materials are beginning to challenge its dominance.[4–6] The biocompatibility and chemical stability of Si are low, and complex strategies are required to design Si-based biosensors. Furthermore, Si-based electronic devices for sensing applications suffer from relatively high noise, which limits the device sensitivity.[3] More recently, carbon nanotube[7,8] and nanowire[9,10] field-effect transistors were shown to be very promising candidates for the electrical detection of chemical and biological species. However, despite the excellent performance of individual sensors, the poor device reproducibility and difficulties of large-scale integrated processing of CNTs and nanowires pose major obstacles for the success of these technologies.

In contrast, graphene possesses extraordinary material properties which should enable it to surpass both Si and CNT-based technologies for biosensors and bioelectronics.[11,12] Compared to Si, graphene shows superior chemical stability, and is expected to be bio-inert. In addition, the electrical properties of graphene allow it to outperform Si for sensing devices: graphene is an ideal two-dimensional system which shows very high mobilities of both holes and electrons even at room temperature,[11–14] and is electrically sensitive to environmental conditions and charge adsorption.[15,16] Highly sensitive gas sensors, down to the single molecule limit, have been demonstrated using graphene field-effect transistors, confirming the enormous potential of this material in such applications.[17,18] Furthermore, the demonstration of scalable epitaxial growth of graphene on SiC[19–21] and metal substrates[22,23] offers new prospects for graphene-based devices.

So far, most of the reports on graphene field-effect transistors have addressed operation under vacuum or atmospheric conditions. Only very recently, the operation of graphene in aqueous electrolytes, for potential use in biosensors and bioelectronics, has been reported by a few groups.[24,25] The use of solution-gated epitaxial graphene as a pH sensor was first demonstrated by Loh et al.[24] Ohno et al. recently reported on electrolyte-gated graphene field-effect transistors for detecting pH and protein adsorption.[25] These two works already confirm the potential of graphene for sensing in aqueous electrolytes.

[*] M. Dankerl, M. V. Hauf, A. Lippert, L. H. Hess, S. Birner, Dr. I. D. Sharp, Prof. Dr. M. Stutzmann, Dr. J. A. Garrido
Walter Schottky Institut
Technische Universität München
Am Coulombwall 3, 85748 Garching (Germany)
E-mail: garrido@wsi.tum.de

Dr. A. Mahmood, Dr. P. Mallet, Dr. J.-Y. Veuillen
Institut Néel
CNRS-Université Joseph Fourier
Boîte Postale 166, F-38042
Grenoble Cedex 9 (France)

DOI: 10.1002/adfm.201000724

 © 2010 WILEY-VCH Verlag GmbH & Co. KGaA, Weinheim

However, a detailed understanding of the graphene/electrolyte interface, the effect of the electrolyte on the electronic transport in graphene, as well as standard bench-marks such as low-frequency noise and reliability, are still lacking.

Here, we provide direct determination of charge carrier mobilities and concentrations as a function of electrolyte gate potential using novel in-solution Hall-effect measurements and analyze the results by taking into account the microscopic structure of water at the interface. Furthermore, we report on the fabrication and operation of reliable solution-gated field effect transistor arrays from scalable epitaxial graphene, demonstrating a performance which is superior to currently available technologies in terms of both noise and sensitivity.

2. Results and Discussion

Because of its proven scalability,[20] epitaxial graphene was chosen for fabrication of solution-gated field effect devices. Growth was achieved on the (0001) Si face of semi-insulating 6H-SiC by thermal decomposition at 1200 °C under ultra high vacuum (UHV) conditions and was confirmed by examining the low-energy electron diffraction (LEED) patterns upon annealing (see experimental section).[26,27] In situ STM images of large areas (see Supporting Information) reveal terraces with lateral sizes between 10 and 100 nm, typical of the UHV graphitized Si-face of SiC.[19,26,27] Monolayer graphene (ML) can be identified through the interface contribution which appears as a (6 × 6) modulation in high bias images (**Figure 1a**) and through the honeycomb contrast in low bias images with atomic resolution (see Supporting Information).[26] Auger spectra taken in-situ at different spots on the substrate separated by several mm also suggest an average graphene thickness between 1 ML and 1.5 ML which is homogeneous over large areas. The graphene SGFET devices were fabricated using UV-photolithography (see experimental section): transistors with different gate areas (40 μm × 10 μm and 40 μm × 20 μm) were processed around the sample center, where a van der Pauw structure of 700 μm × 700 μm was fabricated for in-electrolyte Hall-effect measurements (Figure 1b).

Using the concept of an ideally polarizable electrode/electrolyte interface the modulation of the conductivity and carrier concentration with the electrolyte potential is schematically shown in Figure 1c, in which the applied gate voltage fixes the potential drop between E_F in the graphene and the reference electrode, and thus the density and type of the charge carriers. **Figure 2a** shows the effective modulation of the graphene conductivity by the electrolyte potential; henceforth, the electrolyte potential will be referred to as gate potential (U_G) and the electrolyte potential at the minimum of the conductivity–U_G curve will be referred to as the Dirac point (U_D). The conductivity, calculated from the 4-point resistivity measurements performed using the van der Pauw structure, exhibits the expected V-shape consistent with the semimetal nature of graphene.

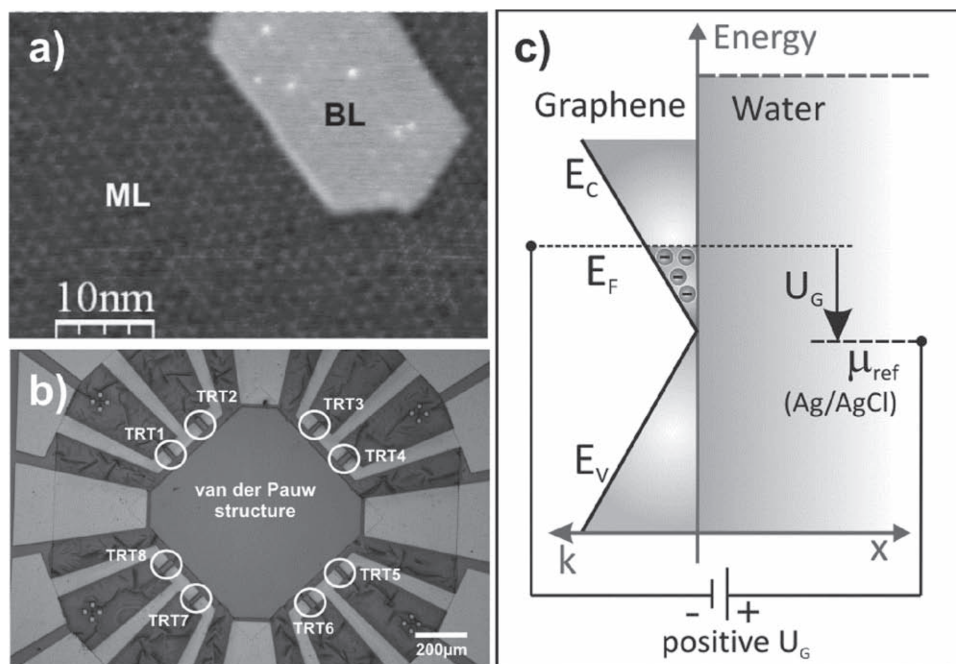

Figure 1. Fabrication and operation of graphene solution-gated field effect transistors. a) In-situ STM image revealing the morphology of the as-grown epitaxial graphene. It consists of large terraces covered with single layer graphene (ML) showing a pronounced modulation with (6 × 6) periodicity (with respect to SiC) characteristic of monolayer graphene on SiC(0001). Patches of bilayer islands (BL) with smaller corrugation are also found on the surface. Image size: 50 mm × 36 nm, sample bias: –0.5 V, tunneling current: 0.2 nA. b) Optical microscopy image of graphene SGFETs. The Ti/Au structures (bright) represent drain and source contacts for the transistors (gate areas of 40 μm × 10 μm and 40 μm × 20 μm) and contacts for the van der Pauw structure in the centre. c) Schematic drawing representing the modulation of the carrier density in the graphene film: the applied gate voltage (with respect to the reference electrode) shifts the Fermi level in graphene above (shown) or below the Dirac point, thus modulating the number of free carriers.

© 2010 WILEY-VCH Verlag GmbH & Co. KGaA, Weinheim

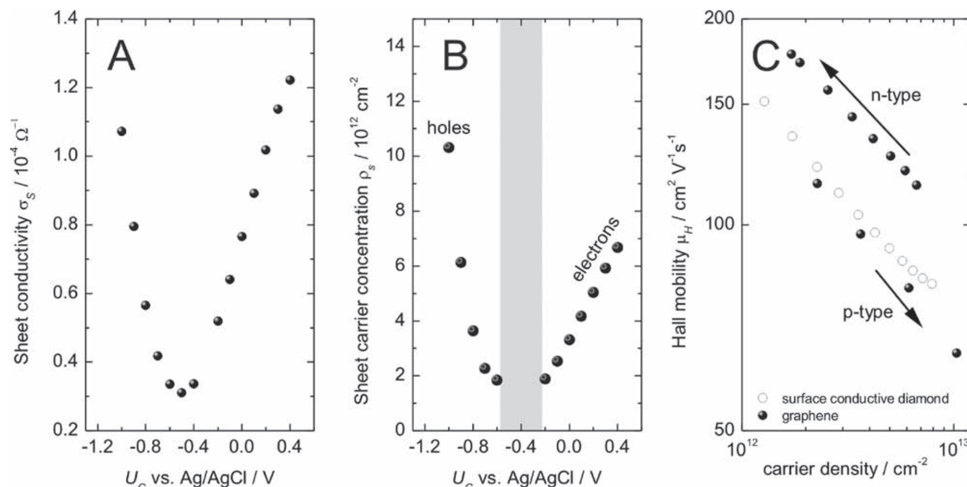

Figure 2. Electrolyte-gating of graphene. A) Sheet conductivity derived from the 4-point resistivity measurements performed using the van der Pauw structure. The minimum of the conductivity occurs at a gate potential of –0.5 V versus the Ag/AgCl reference electrode. B) Carrier concentration versus gate voltage calculated from the 4-point Hall-effect experiments. Close to the Dirac point, it is not possible to estimate the number of carriers. The curve exhibits a clear asymmetry around the Dirac point. C) Hall mobility versus carrier concentration. For comparison, we include the mobility-carrier density dependence of diamond solution gate field effect structures, in which a 2D hole gas is formed at the surface of a hydrogenated diamond. A clear asymmetry around the Dirac point is revealed, with electrons showing a higher mobility than holes. For both electrons and holes, the Hall mobility decreases with increasing carrier concentration, following a power law in which $\mu \approx n^{-0.3}$.

In addition, we have performed Hall-effect measurements under electrolyte gate control in order to directly determine the carrier charge, density, and mobility as a function of the applied gate potential (see the Experimental Section). Figure 2b shows the variation of the sheet carrier concentration as a function of U_G in which three regions should be considered: for $U_G > U_D$ a quasi-linear relationship between the electron density and U_G is observed; for $U_G < U_D$, on the other hand, a supralinear dependence between the hole density and U_G is observed. Near the Dirac point, the estimation of the carrier concentration becomes difficult, since the Hall voltage goes to zero when the number of holes and electrons is similar. In any case, the estimated carrier density near the Dirac point, which is about 10^{12} cm^{-2}, can be considered an upper limit. Ideally, for SL graphene, a concentration of about 10^{11} cm^{-2} holes and electrons is expected at the Dirac point at room temperature.[11] We note that the presence of charged impurities can induce chemical doping, increasing significantly the number of carriers and shifting the Fermi level away from the Dirac point in the absence of a gate potential. Furthermore, it has been shown that the built-in electric field at the graphene/SiC interface can result in electron doping of the graphene layers.[19,20,28,29]

In order to fully understand the modulation of the carrier density in graphene with the electrolyte potential we have to consider the charge distribution at the graphene/electrolyte interface. An electrical double layer is expected to form at an ideally polarizable electrode/electrolyte interface. For carbon-based electrodes, this interfacial layer is typically described by a double layer capacitance (C_{DL}) with values varying from a few µF cm^{-2} (for diamond electrodes[30]) to a few tens of µF cm^{-2} (for graphite electrodes[31]). In the case of graphene, in addition to the double layer capacitance, the so-called quantum capacitance (C_Q) must be considered. C_Q is defined as $\partial Q/\partial U_{gr}$, where $Q = e(p–n)$ corresponds to the total charge in graphene and U_{gr} represents the electrostatic potential in graphene, i.e. the position of the Fermi level in graphene with respect to the Dirac point.[32–34] Therefore, for the case of graphene both the quantum capacitance and the double layer capacitance contribute to the total interfacial capacitance. Thus, the applied gate voltage cannot be directly assigned to the electrostatic potential in graphene, since part of the applied voltage drops in the electrolyte close to the graphene surface. We note that previous studies have relied on a description of the bulk electrolyte using a homogeneous dielectric constant of water of about $\varepsilon = 78\varepsilon_0$, which can lead to a significant overestimation of the double layer capacitance.[24,25] In order to model the graphene/electrolyte interface, two different descriptions of the electrolyte have been used. In the first model, we assume an electrolyte with a homogeneous static dielectric constant of $\varepsilon_r = 78$, in which ions are described by a Poisson–Boltzmann (PB) distribution. It is well known that the Poisson–Boltzmann modelling of an electrolyte suffers from several limitations. Thus, our second model considers a spatially varying static dielectric constant $\varepsilon_r(x)$ for water based on molecular dynamic simulations,[35] which takes into account the structuring of water in the vicinity of a nonpolar (hydrophobic) solid wall. Additionally, we use an extended Poisson–Boltzmann (ePB) equation which includes for each ion (i = Na^+, Cl^-) a spatially varying potential of mean force (PMF) using the parameterization suggested by Schwierz et al. for hydrophobic interfaces.[35] The PMFs are only relevant in the vicinity of the interface (0 nm to 1.4 nm), and introduce a repulsive term which prevents the unphysical situation of ions coming too close to the graphene surface. Using the next**nano** software,[36] we calculated self-consistently the spatial charge and electrostatic potential distributions in the graphene/electrolyte system by solving the nonlinear Poisson equation,[37] in which a spatially varying static dielectric function $\varepsilon_r(x)$ can be considered. The ion distribution in the electrolyte is calculated

© 2010 WILEY-VCH Verlag GmbH & Co. KGaA, Weinheim

as described above. The sheet charge density in graphene is calculated according to Fang et al.,[33] assuming a linear energy dispersion E(**k**) for isolated graphene. A detailed description of the simulations is given in the Supporting Information.

Using this model we have evaluated the carrier densities in graphene and the ion densities in the electrolyte at the graphene/electrolyte interface. **Figure 3a** shows the potential profile across the graphene/electrolyte interface for different U_G values. In the case of the PB model, with a static dielectric constant $\varepsilon = 78\varepsilon_0$, the potential drop in the electrolyte region is very small, so that the applied gate voltage nearly directly changes the Fermi level in the graphene layer. On the other hand, in the case of the ePB model, a strong potential drop is observed in the vicinity of the graphene/electrolyte interface, which results in a lower value of the electrostatic potential in the graphene layer. Figure 3b shows the carrier density calculated based on the previous models; the carrier density expected from the quantum limit in graphene ($U_G = E_F/e$) is shown for comparison, together with the experimental results obtained from the Hall measurements. This comparison confirms that the graphene/electrolyte interface cannot be solely described by the quantum capacitance, since the experimental carrier density is much smaller than predicted by the quantum limit. Furthermore, the PB model cannot describe the experimental results; the double layer capacitance predicted by this model is too high, and therefore the situation is similar to the quantum limit. Finally, the carrier density predicted by the ePB model, which accounts for the microscopic structure of water near the interface with no fitting parameters, is in reasonable agreement with the experimental results. We note that the electron-hole asymmetry found experimentally (Figure 3b) cannot be understood with this model. Other considerations, such as bilayer graphene with its different effective mass for electrons and holes,[38] or chemical doping by ion adsorption,[24] could possibly explain this effect.

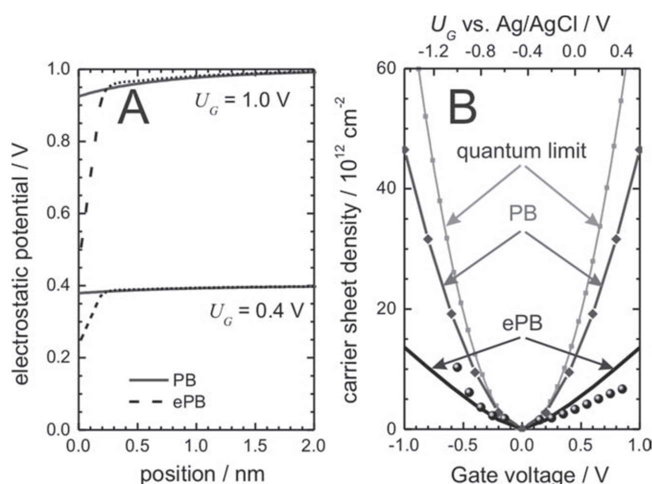

Figure 3. Modeling the graphene/electrolyte interface. Results of the simulation of the graphene/electrolyte interface in which the electrolyte is described by i) a Poisson-Boltzmann (PB) distribution and a homogeneous static dielectric constant, corresponding to bulk water $\varepsilon_r = 78$, and ii) an extended Poisson-Boltzmann (ePB) model including a local dielectric constant and a local potential of mean forces for the ions. A) Variation of the electrostatic potential across the graphene/electrolyte interface, for two different values of U_G revealing a significant potential drop in the electrolyte. Only results for $U_G < U_D$ are shown; for $U_G > U_D$ the results are symmetric with respect to the potential axis. B) Carrier density versus applied gate voltage obtained for the two different models, together with the "quantum limit" situation, i.e., $E_F^{graphene} = eU_G$. The experimental results (*x*-axis has been shifted so that $U_D = 0$ V) are included for comparison. In the case of the PB model, the potential drop in the electrolyte is almost negligible, i.e. the electrostatic potential in graphene approximately equals U_G, resembling the "quantum limit" situation. In the case of the ePB model, an important potential drop occurs in the electrolyte, which strongly reduces the electrostatic potential in the graphene film.

Using the resistivity and carrier density determined directly from in-solution Hall-effect measurements, the dependence of the carrier mobility on the electrolyte gate potential and carrier density can be evaluated (Figure 2c). It is observed that the Hall mobility decreases with increasing carrier density. The magnitude of the mobility is in good agreement with values for epitaxial graphene prepared on the Si-face of SiC, where low carrier mobilities are typically reported.[21,39] There is also a clear asymmetry for hole and electron mobilities: at the same carrier concentration, the electron mobility is noticeably higher than the hole mobility. Although the influence of charged impurities on transport in graphene is widely acknowledged, the limiting scattering mechanism is still a matter of discussion.[40–42] It has been suggested that Coulomb scatterers present at the graphene/substrate interface, or even adsorbed on the graphene surface limit the carrier mobility. Theory predicts that long-range Coulomb scattering, such as that due to charged impurities in the vicinity of graphene, will lead to carrier mobilities which are independent of the carrier density.[40,41] On the other hand, short-range scattering, such as that due to point defects or ripples in the film, is predicted to decrease the mobility with increasing carrier density.[40,42,43] Recently, Tedesco et al. have reviewed the dependence of the Hall mobility on the carrier density in epitaxial graphene on SiC.[39] For graphene grown on the Si-face of SiC, the mobility strongly decreases with the increase in carrier concentration (both electrons and holes), almost following a $\mu \approx n^{-1}$ dependence. It was suggested that the relationship between carrier mobility and carrier concentration may result from the stepped morphology of graphene due to the underlying SiC substrate, and is an intrinsic characteristic of epitaxial graphene synthesized by the sublimation method.[39] As can be seen in Figure 2c, our experiments do not reproduce such a trend; instead, the mobility exhibits a weaker dependence on the carrier concentration, following $\mu \approx n^{-0.3}$. However, we note that the exact dependence of the mobility on the carrier density, as theoretically predicted for ripple-induced scattering, strongly depends on the surface morphology, and it has been shown to vary from an almost constant value to a $\mu \approx n^{-1}$ dependence.[40,42] In our specific case, in which the graphene film is in contact with an aqueous electrolyte, additional Coulomb scattering is expected due to the double layer formed at the graphene/electrolyte interface. As shown in the Supporting Information, the ion density in the vicinity of the graphene depends on the carrier density, due to the charge neutrality requirement. Therefore, even if the ions are treated as long-range Coulomb scatterers, the mobility is expected to decrease with increasing carrier density, due to the correspondingly increased density of ionic scattering centers. Additional scattering mechanisms related to the

© 2010 WILEY-VCH Verlag GmbH & Co. KGaA, Weinheim

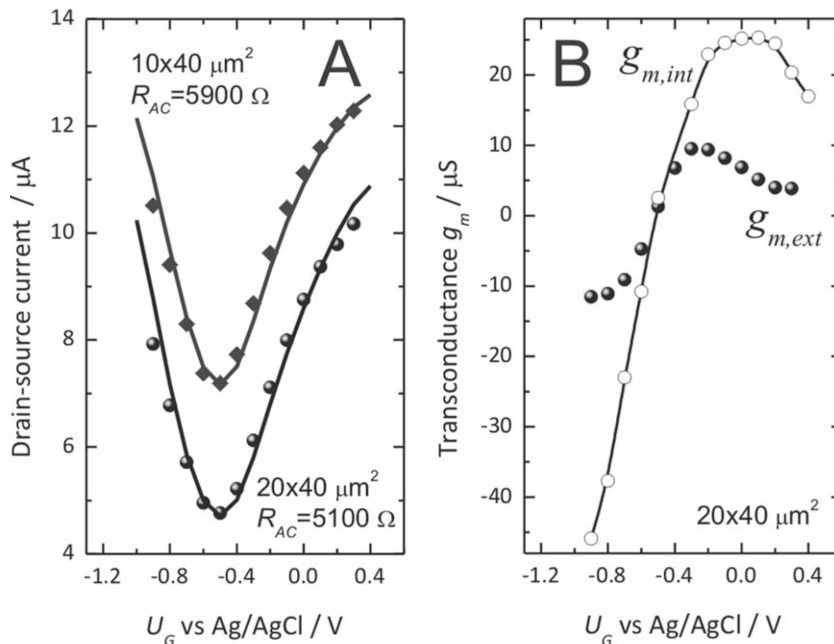

Figure 4. Characterization of graphene SGFETs in electrolyte. A) Drain-source current curves (for U_{DS} = 100 mV) measured (solid symbols) at different gate voltages, for two graphene transistors with different active area 10 μm × 40 μm and 20 μm × 40 μm. The solid line represents the estimation of the drain-source current from the 4-point resistivity measurements and the contribution of the access resistance. B) Effect of the access resistance on the transconductance. The solid symbols correspond to the so-called extrinsic transconductance, i.e., $\partial I_{DS}/\partial U_G$, which represents the modulation capability of the gate. Due to the effect of the access resistance, the extrinsic transconductance is strongly reduced with respect to the intrinsic transconductance.

graphene/aqueous electrolyte interface could also be relevant, such as interface dipole scattering introduced by structuring of water in contact with the hydrophobic surface of graphene. In Figure 2c, we compare the mobility-carrier density dependence of the graphene SGFET with that of diamond SGFET devices, in which a 2D hole gas is formed at the surface of a hydrogenated diamond.[44,45] The similarity between both sets of data is striking and may suggest a common origin of the scattering mechanism induced by the solid/electrolyte interface. Further experiments are planned to conclusively identify the main scattering mechanisms in graphene SGFETs.

The characteristics of two micrometer-scaled SGFETs (10 μm × 40 μm and 20 μm × 40 μm) are shown in **Figure 4a**. The symbols correspond to the measured drain-source current at a constant U_{DS} = 100 mV as a function of the gate voltage (see the Experimental Section). The solid lines have been derived (see the Supporting Information) from the 4-point conductivity measurements and consider the series resistance due to the access region resulting from the fabrication method. This access region, which cannot be modulated by the gate potential, corresponds to that part of the graphene film between drain and source which is covered with the chemically insulating SU-8 resist. Figure 4a shows an excellent agreement between the measured drain source current and the calculated current. It is worth recalling that the calculated current is based on the resistivity measurements, which are performed using a van der Pauw structure of large dimensions (700 μm × 700 μm). On the other hand, the characterized transistors have much smaller dimensions (down to 10 μm × 40 μm) and can be separated by more than 1 mm, highlighting the homogeneity of the graphene film and confirming the potential of epitaxial graphene for large scale device production.

One of the key parameters characterizing the sensitivity of a FET is the transconductance, i.e., the I_{DS} modulation induced by a small U_G variation. While the change of current relative to its absolute value is in general higher for transistors operated in the subthreshold regime, the device should be operated at the point of maximum transconductance, where the ratio between amplified signal and noise is maximized for each device. This signal-to-noise ratio will determine the final sensitivity of the device. It can be easily shown that the access resistance limits the maximum transconductance of the device. Figure 4b shows the transconductance calculated from the I_{DS}-U_G curves of the 20 μm × 40 μm transistor in Figure 4a, which we refer to as the extrinsic transconductance ($g_{m,ext}$). For comparison, we include the so-called intrinsic transconductance ($g_{m,int}$), which is calculated from the resistivity measurements after correction for the access resistance. As the graph shows, the access resistance reduces the transconductance maximum by a factor of 3. By using an improved transistor design with a reduced access region length, the $g_{m,ext}$ will approach $g_{m,int}$. Furthermore, improving the carrier mobility via advanced and rapidly improving growth techniques will also result in a significant increase of $g_{m,int}$.

In addition to the transconductance, the low-frequency noise of a graphene transistor will have a major influence on its sensitivity.[46] **Figure 5a** shows the current noise spectral density measured as described in the experimental section. For all measured devices, we have found a $1/f$ dependence of the current noise spectral density, where f is the frequency. $1/f$ noise in electronic devices is often characterized by the empirical Hooge law,[47] in which the noise scales inversely with the number of carriers (N) contributing to the electronic transport, following

$$S_{I_{DS}} = \frac{\alpha_H}{N}\frac{1}{f}I_{DS}^2 \quad (1)$$

Here, α_H is the so-called Hooge parameter, often used to characterize the noise properties of electronic conductors like metals and semiconductors. For device characterization, the number of carriers is often not known, and the noise amplitude $A = \alpha_H/N$ is thus used to assess the noise performance. We find that the current noise density is proportional to the current squared, indicating that the $1/f$ noise is due to resistance fluctuations. Figure 5b shows the gate voltage dependence of the calculated noise amplitude, together with the U_G-dependent resistance (solid line) for one of the devices, revealing a maximum at the Dirac point. This is not unexpected, since the number of carriers, N, has a minimum at the gate voltage corresponding to the Dirac point.

© 2010 WILEY-VCH Verlag GmbH & Co. KGaA, Weinheim

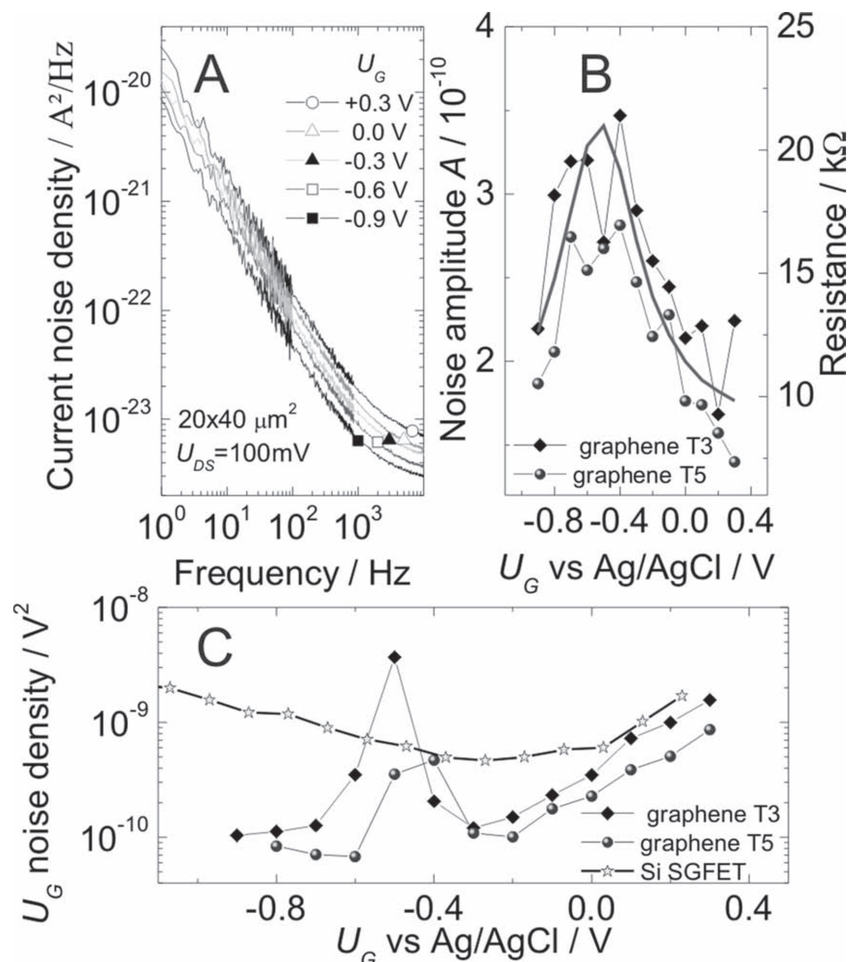

Figure 5. Low-frequency noise characterization. A) Current noise density versus frequency curves measured for a graphene SGFET in electrolyte, at different gate voltages. In the low frequency range, the noise spectra follow a $1/f$ dependence. B) Gate voltage dependence of the noise amplitude A defined as α_H/N (see Equation (1)), where N is the total number of carriers. For comparison, the resistance curve of one of the transistors (T3) is shown (solid line). As described in the text, the noise amplitude has a maximum at the Dirac point, where N exhibits its minimum. C) Gate noise density of the graphene SGFETs compared to Si SGFETs. Due to the minimum of the transconductance close to the Dirac point, the gate noise exhibits a maximum in this gate voltage region. Away from this maximum, the graphene SGFETs exhibit a RMS gate noise of ≈20 μV.

However, in order to properly calculate the Hooge parameter, the contribution of the access resistance must be considered. A detailed discussion of the limitation in the calculation of α_H is provided as Supporting Information. The values of the noise amplitude shown in Figure 5b are in good agreement with recent reports on low-frequency noise in graphene devices.[46,48,49]

With respect to the device sensitivity, the relevant noise parameter to be assessed is the gate voltage noise spectral density, which determines the minimum gate signal that will be detected by the device. For instance, the gate signal can be the action potential of a nerve cell in the proximity of the transistor, or the surface charge modulation induced by a local pH variation. The relation between the gate voltage noise density and the current noise density is given by $S_{U_G} = S_{I_{DS}}/g_m^2$, where g_m represents the extrinsic transistor transconductance. Figure 5c shows the gate voltage noise power density of the transistors in Figure 5b. The maximum at the Dirac point results from the minimum of the transconductance at this gate potential. From the minimum of the gate voltage noise power density, and considering the typical bandwith used in biosensors and bioelectronic applications (1 Hz to 5 kHz), we estimate the RMS of the noise at the gate to be ≈20 μV. This value is nearly one order of magnitude lower than in standard Si-devices used in biosensors, and as low as those of ultralow-noise Si devices currently used in bioelectronic applications.[3] The graphene SGFET intrinsically omits some sources of noise, such as defects at the interface to an oxide, by being directly exposed to an electrolyte. Of course, the electrolyte interface itself, as well as the SiC interface, remain as sources of noise. Therefore, the noise performance of the graphene SGFET devices presented here might differs from graphene devices using solid gates.[50]

Since the extrinsic transconductance can be significantly increased by straightforward reduction of the access region length and by larger carrier mobilities, future electrolyte-gated graphene biosensors have the potential to greatly outperform existing technologies.

3. Conclusions

Indeed, our results strongly indicate that graphene-based SGFETs can set a new paradigm in biosensing and bioelectronics, enabled by their high sensitivity (transconductance) and low noise properties, together with the reliability and scalability demonstrated for epitaxial graphene. Furthermore, the ambipolar character of the devices may enable novel ways of addressing the study of the solid/liquid interface. However, important challenges must be overcome before graphene SGFETS are available for biosensor applications. Among others, we highlight the interaction of organic and bioorganic molecules with graphene surfaces. For biosensors and bioelectronics, surface modification in a controlled way is a mandatory step in order to introduce chemical specificity, as well as to modify the surface reactivity. Developing methods of functionalization with selective biomolecules and understanding the effects of these modifications on the electronic properties of single and multilayer graphene, without doubt, constitute extremely rich and interesting fields which remain to be explored.

4. Experimental Section

Grapheme preparation: Epitaxial graphene was prepared on the Si face of a semi-insulating 6H-SiC substrate purchased from Norstel AB (Sweden) and chemico-mechanically polished by NovaSiC (France)

© 2010 WILEY-VCH Verlag GmbH & Co. KGaA, Weinheim

to an RMS roughness of ~0.2 nm. Following polishing, samples were thoroughly cleaned in solvents and were subjected to two cycles of plasma oxidation and etching in 5% HF for 5 min. Growth was achieved using an ultrahigh vacuum setup equipped with low-energy electron diffraction (LEED), Auger, and scanning tunneling spectroscopy. The semi-insulating [0001] 6H-SiC was first annealed at 900 °C under low Si flux, which produces a [3 × 3] Si-rich phase. Further annealing at 1100 °C resulted in the C-rich phase of the so-called [6 √3 × 6 √3]R30° reconstruction. Final graphitization was achieved at 1200 °C.

Device fabrication: The graphene SGFET device array was fabricated using optical lithography, as follows. A Ti/Au layer stack (10 nm/100 nm) was evaporated to form bond pads and leads to the active area. Prior to the metal evaporation, the open areas were defined by selective etching in an oxygen plasma. In this way, the graphene layer was fully removed from the contact area, improving the adhesion of the Ti/Au layer to the SiC substrate. The active graphene areas of the transistors were defined by etching the surrounding graphene regions using an oxygen plasma. In order to contact the active area of the FETs and form drain and source contacts, an additional Au layer (100 nm) was deposited on the leads, partly overlapping the graphene active region. To prevent the direct contact between the electrolyte and the metal contacts, the entire sample was covered with two subsequent layers (1.5 μm each) of a chemically stable photoresist (SU-8), which were opened at the gate area by optical lithography. Transistors with two different gate areas (width × length: 40 μm × 10 μm and 40 μm × 20 μm) were processed around the sample center, where a van der Pauw structure of 700 μm × 700 μm was fabricated for Hall-effect measurements [Figure 1b]

Resistivity and Hall Effect Measurements: The sheet resistivity and the Hall effect measurements were performed with the graphene sample in electrolyte solution under control of the gate potential. The gate potential was controlled with a potentiostat in a three electrode electrochemical cell with a Ag/AgCl reference electrode, a platinum wire counter electrode and one of the four contacts of the van der Pauw structure connected as a working electrode. All potentials applied between the contacts during measurements were grounded with respect to this working electrode. A 5 mM phosphate buffer adjusted to an ionic strength of 100 mM with NaCl was used as electrolyte. Probe voltages for both the sheet resistivity and Hall effect measurements were ac with a frequency of 1 Hz, making use of lock-in amplifiers for both signal generation and measurement. The applied voltages between the contacts were 50 mV maximum to guarantee a homogeneous gate potential distribution across the sample. The sheet resistivity was measured and evaluated according to the method by van der Pauw, permuted through all four contacts. The Hall-effect measurements were executed similarly, with the contacts also permutated in order to achieve higher accuracy. A 2 T magnetic field was provided by a standard coil magnet and field controller.

Transistor Characteristics Measurements: Transistor characteristics were investigated using a two electrode electrochemical cell, with a Ag/AgCl reference electrode and the source contact of the device as the working electrode. A 10 mM phosphate buffer adjusted to an ionic strength of 50 mM with KCl was used as an electrolyte. The drain-source voltage was applied by a voltage source. The gate voltage was applied using a second voltage source, which sets the potential of the source contact with respect to the reference electrode.

Low-Frequency Noise Measurements: For the low-frequency noise measurements, transistors were biased in a two-electrode setup in which the drain-source and gate voltages were applied by a battery-powered setup. The drain-source current was amplified ($\times 10^5$) with a battery-powered low-noise current pre-amplifier (DL Instruments Model 564). This setup was shielded against external noise with a Faraday cage. Another battery-powered low-noise amplifier (EG&G Parc Model 113) was used to filter frequencies lower than 0.1 Hz and higher than 300 kHz. The noise power spectral density was measured with a spectrum analyzer in a frequency range of 1 Hz to 100 kHz.

Supporting Information

Supporting Information is available from the Wiley Online Library or from the author.

Acknowledgements

We are thankful to A. Offenhäusser (FZ Jülich) for providing the Si-based SGFETs, and to R. R. Netz and N. Schwierz for their help with the parameterization of the potential of mean force of ions and the spatially dependent dielectric constant. This work has been financially supported by the Nanosystems Initiative Munich (NIM), the International Graduate School of Science and Engineering (IGSSE) of the Technische Universität München, the Technische Universität München – Institute for Advanced Study funded by the German Excellence initiative, and the EU through the project Diamond to Retina Artificial Microinterface Structures (DREAMS, FP6-NMP-2006–676033345). M. H. thanks Elitenetzwerk Bayern (CompInt, Material Science of Complex Interfaces) for financial support.

Received: April 15, 2010
Published online: August 4, 2010

[1] P. Fromherz, A. Offenhäusser, T. Vetter, J. Weis, *Science* **1991**, *252*, 1290.
[2] E. Stern, J. F. Klemic, D. A. Routenberg, P. N. Wyrembak, D. B. Turner-Evans, A. D. Hamilton, D. A. LaVan, T. M. Fahmy, M. A. Reed, *Nature* **2007**, *445*, 519.
[3] M. Voelker, P. Fromherz, *Small* **2005**, *1*, 206.
[4] W. Yang, *Nat. Mater.* **2002**, *1*, 253.
[5] A. Hartl, E. Schmich, J. A. Garrido, J. Hernando, S. C. R. Catharino, S. Walter, P. Feulner, A. Kromka, D. Steinmuller, M. Stutzmann, *Nat. Mater.* **2004**, *3*, 736.
[6] M. Dankerl, S. Eick, B. Hofmann, M. Hauf, S. Ingebrandt, A. Offenhausser, M. Stutzmann, J. A. Garrido, *Adv. Funct. Mater.* **2009**, *19*, 2915.
[7] J. Kong, N. R. Franklin, C. W. Zhou, M. G. Chapline, S. Peng, K. J. Cho, H. J. Dai, *Science* **2000**, *287*, 622.
[8] R. J. Chen, S. Bangsaruntip, K. A. Drouvalakis, N. W. S. Kam, M. Shim, Y. M. Li, W. Kim, P. J. Utz, H. J. Dai, *Proc. Natl. Acad. Sci. USA* **2003**, *100*, 4984.
[9] Y. Cui, Q. Q. Wei, H. K. Park, C. M. Lieber, *Science* **2001**, *293*, 1289.
[10] N. Misra, J. A. Martinez, S. C. J. Huang, Y. M. Wang, P. Stroeve, C. P. Grigoropoulos, A. Noy, *Proc. Natl. Acad. Sci. USA.* **2009**, *106*, 13780.
[11] A. H. Castro Neto, F. Guinea, N. M. R. Peres, K. S. Novoselov, A. K. Geim, *Rev. Mod. Phys.* **2009**, *81*, 109.
[12] A. K. Geim, K. S. Novoselov, *Nat. Mater.* **2007**, *6*, 183.
[13] K. S. Novoselov, A. K. Geim, S. V. Morozov, D. Jiang, Y. Zhang, S. V. Dubonos, I. V. Grigorieva, A. A. Firsov, *Science* **2004**, *306*, 666.
[14] K. I. Bolotin, K. J. Sikes, J. Hone, H. L. Stormer, P. Kim, *Phys. Rev. Lett.* **2008**, *101*, 096802.
[15] D. B. Farmer, R. Golizadeh-Mojarad, V. Perebeinos, Y. M. Lin, G. S. Tulevski, J. C. Tsang, P. Avouris, *Nano Lett.* **2009**, *9*, 388.
[16] E. H. Hwang, S. Adam, S. Das Sarma, *Phys. Rev. B* **2007**, *76*, 195421.
[17] F. Schedin, A. K. Geim, S. V. Morozov, E. W. Hill, P. Blake, M. I. Katsnelson, K. S. Novoselov, *Nat. Mater.* **2007**, *6*, 652.
[18] Y. P. Dan, Y. Lu, N. J. ybert, Z. T. Luo, A. T. C. Johnson, *Nano Lett.* **2009**, *9*, 1472.
[19] K. V. Emtsev, A. Bostwick, K. Horn, J. Jobst, G. L. Kellogg, L. Ley, J. L. McChesney, T. Ohta, S. A. Reshanov, J. Rohrl, E. Rotenberg, A. K. Schmid, D. Waldmann, H. B. Weber, T. Seyller, *Nat. Mater.* **2009**, *8*, 203.
[20] W. A. de Heer, C. Berger, X. S. Wu, P. N. First, E. H. Conrad, X. B. Li, T. B. Li, M. Sprinkle, J. Hass, M. L. Sadowski, M. Potemski, G. Martinez, *Solid State Commun.* **2007**, *143*, 92.
[21] C. Berger, Z. M. Song, T. B. Li, X. B. Li, A. Y. Ogbazghi, R. Feng, Z. T. Dai, A. N. Marchenkov, E. H. Conrad, P. N. First, W. A. de Heer, *J. Phys. Chem. B* **2004**, *108*, 19912.

© 2010 WILEY-VCH Verlag GmbH & Co. KGaA, Weinheim

FULL PAPER

[22] P. W. Sutter, J. I. Flege, E. A. Sutter, *Nat. Mater.* **2008**, *7*, 406.
[23] J. Wintterlin, M. L. Bocquet, *Surface Science* **2009**, *603*, 1841.
[24] P. K. Ang, W. Chen, A. T. S. Wee, K. P. Loh, *J. Am. Chem. Soc.* **2008**, *130*, 14392.
[25] Y. Ohno, K. Maehashi, Y. Yamashiro, K. Matsumoto, *Nano Lett.* **2009**, *9*, 3318.
[26] P. Mallet, F. Varchon, C. Naud, L. Magaud, C. Berger, J. Y. Veuillen, *Phys. Rev. B* **2007**, *76*, 041403.
[27] C. Riedl, U. Starke, J. Bernhardt, M. Franke, K. Heinz, *Phys. Rev. B* **2007**, *76*, 245406.
[28] T. OhtaA. Bostwick, J. L. McChesney, T. Seyller, K. Horn, E. Rotenberg, *Phys. Rev. Lett.* **2007**, *98*, 206802.
[29] J. Kedzierski, P. L. Hsu, P. Healey, P. W. Wyatt, C. L. Keast, M. Sprinkle, C. Berger, W. A. de Heer, *IEEE Trans. Elec. Dev.* **2008**, *55*, 2078.
[30] J. A. Garrido, S. Nowy, A. Härtl, M. Stutzmann, *Langmuir* **2008**, *24*, 3897.
[31] J. P. Randin, E. Yeager, *J. Electrochem Soc.* **1971**, *118*, 711.
[32] S. Luryi, *Appl. Phys. Lett.* **1988**, *52*, 501.
[33] T. Fang, A. Konar, H. L. Xing, D. Jena, *Appl. Phys. Lett.* **2007**, *91*, 092109.
[34] J. L. Xia, F. Chen, J. H. Li, N. J. Tao, *Nat. Nanotech.* **2009**, *4*, 505.
[35] N. Schwierz, D. Horinek, R. R. Netz, *Langmuir* **2010**, *26*, 7370.
[36] S. Birner, T. Zibold, T. Andlauer, T. Kubis, M. Sabathil, A. Trellakis, P. Vogl, *IEEE Trans. Electron Devices* **2007**, *54*, 2137.
[37] S. Birner, C. Uhl, M. Bayer, P. VoglJ. *Phys.: Conf. Ser.* **2008**, *107*, 012002.
[38] E. V. Castro, K. S. Novoselov, S. V. Morozov, N. M. R. Peres, J. M. B. L. Dos Santos, J. Nilsson, F. Guinea, A. K. Geim, A. H. C. Neto, *Phys. Rev. Lett.* **2007**, *99*, 216802.
[39] J. L. Tedesco, B. L. VanMil, R. L. Myers-Ward, J. M. McCrate, S. A. Kitt, P. M. Campbell, G. G. Jernigan, J. C. Culbertson, C. R. Eddy, D. K. Gaskill, *Appl. Phys. Lett.* **2009**, *95*, 122102.
[40] J. H. Chen, C. Jang, S. Adam, M. S. Fuhrer, E. D. Williams, M. Ishigami, *Nature Phys.* **2008**, *4*, 377.
[41] S. Adam, E. H. Hwang, V. M. Galitski, S. Das Sarma, *Proc. Nat. Acad. Sci. USA* **2007**, *104*, 18392.
[42] M. I. Katsnelson, A. K. Geim, *Philos. Trans. R. Soc. London, Ser. A* **2008**, *366*, 195.
[43] T. Stauber, N. M. R. Peres, F. Guinea, *Phys. Rev. B* **2007**, *76*, 205423.
[44] F. Maier, M. Riedel, B. Mantel, J. Ristein, L. Ley, *Phys. Rev. Lett.* **2000**, *85*, 3472.
[45] J. A. Garrido, A. Hartl, M. Dankerl, A. Reitinger, M. Eickhoff, A. Helwig, G. Muller, M. Stutzmann, *J. Am. Chem. Soc.* **2008**, *130*, 4177.
[46] Y. M. Lin, P. Avouris, *Nano Lett.* **2008**, *8*, 2119.
[47] F. N. Hooge, *Phys. Lett. A* **1969**, *29*, 139.
[48] A. N. Pal, A. Gosh, *Phys. Rev. Lett.* **2009**, *102*, 126805.
[49] Q. H. Shao, G. X. Liu, D. Teweldebrhan, A. A. Balandin, S. Runryantsev, M. S. Shur, D. Yan, *IEEE Electron Device Lett.* **2009**, *30*, 288.
[50] Y. M. Lin, P. Avouris, *Nano Lett.* **2008**, *8*, 2119.

© 2010 WILEY-VCH Verlag GmbH & Co. KGaA, Weinheim

Submitted to ADVANCED FUNCTIONAL MATERIALS

Graphene solution-gated field effect transistor array for sensing applications

By *Markus Dankerl*[1], *Moritz V. Hauf*[1], *Andreas Lippert*[1], *Lucas Hess*[1], *Stefan Birner*[1], *Ian D. Sharp*[1], *Ather Mahmood*[2], *Pierre Mallet*[2], *Jean-Yves Veuillen*[2], *Martin Stutzmann*[1], and *Jose A. Garrido*[1]*

[1]Walter Schottky Institut, Technische Universität München, Am Coulombwall 3, 85748 Garching, Germany.
[2]Institut Néel, CNRS-Université Joseph Fourier, Boîte Postale 166, F-38042, Grenoble Cedex 9, France

[*] Author of Correspondence:
Jose A. Garrido
phone: ++49-89 289 12766
e-mail: garrido@wsi.tum.de

Supplementary Information

STM characterization

In-situ STM was used to assess the quality and thickness of the graphene film. STM images of large areas (**Fig. S1a**) reveal terraces with a lateral size between 10 and 100 nm. Small scale STM images at low sample bias (**Fig. S1b**) confirm the presence of mostly a monolayer graphene film. However, as usual for UHV grown samples[19,26,27], patches of the substrate not covered by graphene (0 L) and islands of bilayer graphene (BL) are also observed.

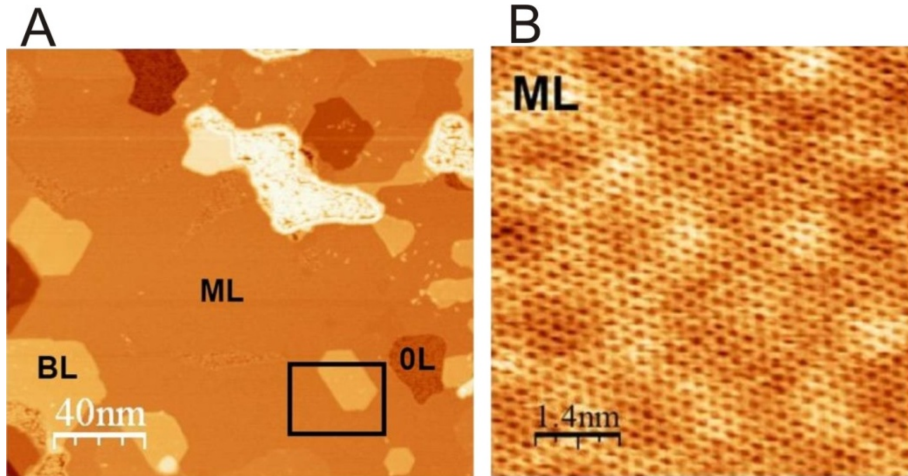

Figure S1. STM characterization of epitaxial graphene. (a) Large scale STM image revealing the morphology of the film, which consists of a large terrace covered with a single layer of graphene (ML). Patches not covered with graphene (0L) and bilayer islands (BL) are also found on the surface. Image size: 200×183 nm², sample bias: -1.0 V, tunneling current: 0.2 nA. A zoomed-in image of the boxed area in (a) is displayed in **Fig. 1a** (in main text). (b) Atomic resolution image taken on the ML phase. It shows the honeycomb contrast expected for monolayer graphene. Image size: 7×7 nm², sample bias: -0.1 V, tunneling current: 0.15 nA.

Impact of access resistance on the transistor characteristics

The characteristics of two micrometer-scaled (10x40 μm^2 and 20x40 μm^2) graphene transistors are shown in **Fig. 4a** (main manuscript). The solid symbols correspond to the measured drain-source current at a constant U_{DS}=100 mV as a function of the gate voltage. The solid lines have been derived from the 4-point conductivity measurements considering the series resistance due to the large access region. This access region, which cannot be modulated by the gate potential, corresponds to that part of the graphene film between drain and source covered with the chemically insulating SU-8 resist; in our transistor design, the access region has a length of 12 μm. The solid lines in **Fig. 4a** are calculated as

$$I_{DS} = \frac{U_{DS}}{\left(R_{AC} + \frac{L}{W}\rho_{vdP}(U_G)\right)} \tag{s1}$$

in which L and W correspond to gate length and width, respectively; ρ_{vdP} (U_G) is the gate voltage dependent resistivity calculated using the van der Pauw design (**Fig. 1b** in main text); R_{AC} corresponds to the access resistance and has been used as a free parameter to fit the measured drain-source current to equation (s1). The calculated currents using equation (s1) are shown in **Fig. 4a**; the estimated access resistances are between 5100 and 5900 Ω. Considering the dimensions of the access region, the estimated access resistances amount to a sheet conductivity of about 0.5-0.6 x 10^{-4} Ω^{-1}. From the van der Pauw measurements, the conductivity minimum is about 0.3 x 10^{-4} Ω^{-1}, suggesting that the deposition of SU8 leads to a weak chemical doping of the underlying graphene film.

Low-frequency noise

The Hooge parameter can be derived from the experimental data, once the contribution of the access resistance is taken into consideration. The total resistance (R_T) fluctuations can be written as

$$\frac{S_{I_{DS}}}{I_{DS}^2} = \frac{S_{R_T}}{R_T^2} = \frac{S_{R_{AC}} + S_{R_{CH}}}{R_T^2} = \frac{A_{AC}}{f}\frac{R_{AC}^2}{R_T^2} + \frac{\alpha_H}{N_{CH} f}\frac{R_{CH}^2}{R_T^2} \tag{s2}$$

in which the subindices AC, and CH refer to access region and channel region, respectively. Thus, the Hooge parameter can be calculated from

$$\alpha_H = \frac{S_{I_{DS}}}{I_{DS}^2} f \frac{R_T^2}{R_{CH}^2} N_{CH} - A_{AC}\frac{R_{AC}^2}{R_{CH}^2} N_{CH} . \tag{s3}$$

Equation (s3) indicates that when the effect of the access resistance is negligible (R_{CH} >> R_{AC}, and $R_T \approx R_{CH}$), the Hooge parameter can be calculated as in equation (1) of the main manuscript. However, when the access resistance becomes dominant, the Hooge parameter

can only be estimated if the noise amplitude corresponding to the access region A_{AC} is known. **Fig. S2** shows the first and the second terms of equation (s3) as a function of the carrier concentration. The second term in equation (s3) is proportional to $(N_{CH})^3$, as given by the dashed line in the figure; note that $R_{CH} \propto 1/N_{CH}$. For the noise amplitude in the second term A_{AC}, we assume the maximum value which can be expected from the data depicted in **Fig. S2**, $A_{AC}=3x10^{-10}$. This is approximately the same noise amplitude which was measured close to the Dirac point (see **Fig. 5** in main text), once the correct geometry factor for the access region is considered. In summary, the Hooge parameter can be estimated to be close to 10^{-2}, not far away from the value obtained for other semiconductors.

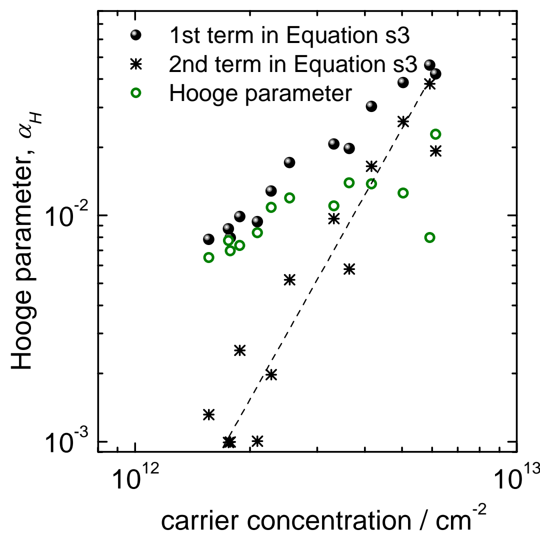

Figure S2. Derivation of the noise Hooge parameter calculated from equation (s3). The figure shows the carrier concentration dependence of the different terms in equation (s3). The solid circles correspond to the first term, representing the measured noise normalized by a factor considering the ratio of the total and channel resistance. The second term corresponds to the contribution of the access resistance to the Hooge parameter and is represented by the star symbols. From equation (s3), it is expected to have a $(N_{CH})^3$ dependence. Open green circles

are the calculated Hooge parameter, once the contribution of the access resistance is considered.

Modelling of the graphene/electrolyte interface

Using the next**nano** software (http://www.nextnano.de) we calculate self-consistently the spatial charge ρ(x) and electrostatic potential ϕ(x) distribution in the graphene/electrolyte system by solving the nonlinear Poisson equation

$$\frac{\partial}{\partial x}\varepsilon_0\varepsilon_\mathrm{r}(x)\frac{\partial}{\partial x}\phi(x)=-\rho(x) \quad \text{(s4)}$$

assuming a spatially varying static dielectric constant $\varepsilon_r(x)$ where ε_0 is the permittivity of vacuum. We used the Dirichlet boundary condition $\phi(\infty) = U_G$ for the electrostatic potential in the bulk electrolyte which is determined by the voltage U_G of the reference electrode (corresponding to zero net ion charge density in the electrolyte far away from the interface), and the Neumann boundary condition $\partial\phi/\partial x = 0$ V/m (vanishing electric field) deep in the graphene layer corresponding to overall charge neutrality.
The sheet charge density in graphene is calculated according to Fang et al.,[36] assuming a linear energy dispersion E(**k**) for bulk graphene leading to electron densities n and hole densities p given by

$$n=\frac{2}{\pi}\left(\frac{k_\mathrm{B}T}{\hbar v_\mathrm{F}}\right)^2 \mathrm{F}_1(+\eta) \quad \text{(S5a)}$$

$$p=\frac{2}{\pi}\left(\frac{k_\mathrm{B}T}{\hbar v_\mathrm{F}}\right)^2 \mathrm{F}_1(-\eta) \quad \text{(S5b)}$$

where the Fermi velocity v_F of the charge carriers in graphene was chosen to be 0.98×10^6 m/s. F_1 is the Fermi-Dirac integral of the order 1 having $\eta=(E_\mathrm{F}-E_\mathrm{D})/k_\mathrm{B}T$ as its argument where the position of the Fermi level E_F relative to the Dirac point E_D determines the charge

fit functions of the potentials of mean force reasonably well at the solid/liquid interface. More details on the simulation of the combined system of semiconductor/electrolyte systems with the next**nano** software are described in Ref. [40].

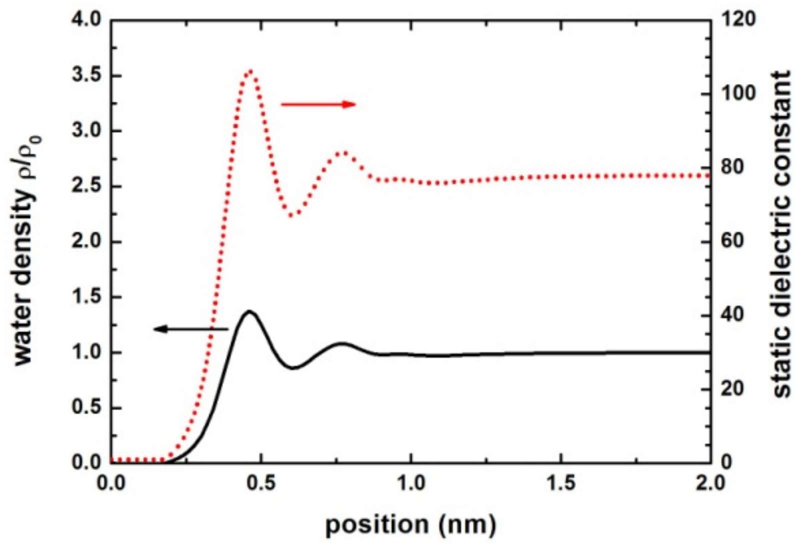

Figure S3. Spatially varying static dielectric constant $\varepsilon_r(x)$ (dotted line) of the electrolyte at a hydrophobic solid/liquid interface according to the parameters of Ref. [38].

Figure S4. Ionic potentials of mean force (PMF) for the ions Na^+ (solid line) and Cl^- (dotted line) at a hydrophobic solid/liquid interface according to the parameters of Ref. [35]. The interface is at 0 nm, and the PMFs are zero beyond 1.4 nm indicated by the vertical line. One can clearly see that the PMFs repel the ions strongly for distances below 0.4 nm from the interface.

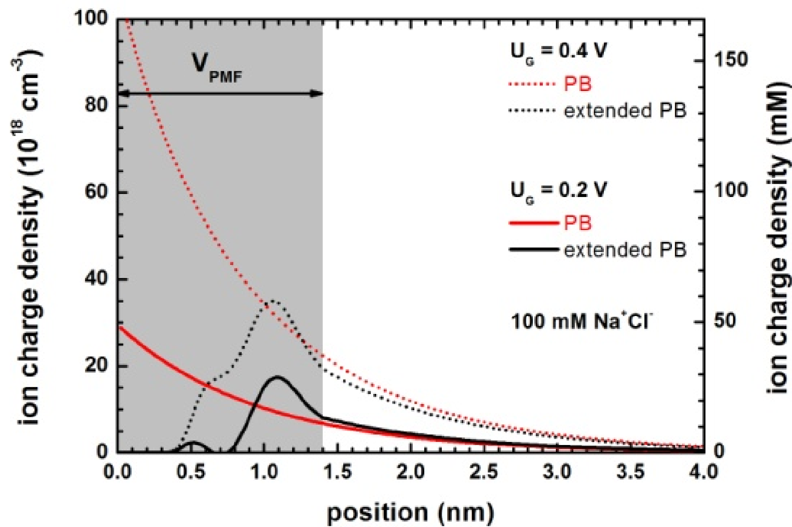

Figure S5. Total ion density profile ρ(x) for U_G = 0.2 V (solid lines) and U_G = 0.4 V (dotted lines) for i) the standard Poisson-Boltzmann model (red lines) and the ii) extended Poisson-Boltzmann model (black lines), which considers a hydrophobic solid/liquid interface. The grey rectangle indicates the region where the potentials of mean force are nonzero.

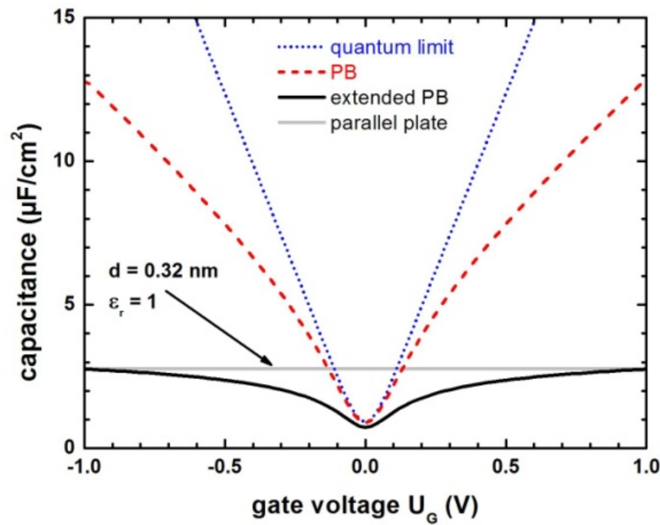

Figure S6. Interfacial capacitance of the graphene/electrolyte system as a function of applied gate electrode potential U_G for the hydrophobic (black solid line) solid/liquid interface (extended Poisson-Boltzmann model). The results of the standard Poisson-Boltzmann approach (red dashed line) are shown for comparison. The blue line shows the quantum limit of bulk graphene where a shift in U_G corresponds directly to a shift of the Fermi level with respect to the Dirac point.